

Fantastic Animals and Where to Find Them: Segment Any Marine Animal with Dual SAM

Pingping Zhang* Tianyu Yan Yang Liu Huchuan Lu

School of Future Technology, School of Artificial Intelligence, Dalian University of Technology, China

2981431354@mail.dlut.edu.cn; {zhpp, ly, lhchuan}@dlut.edu.cn

Abstract

As an important pillar of underwater intelligence, Marine Animal Segmentation (MAS) involves segmenting animals within marine environments. Previous methods don't excel in extracting long-range contextual features and overlook the connectivity between discrete pixels. Recently, Segment Anything Model (SAM) offers a universal framework for general segmentation tasks. Unfortunately, trained with natural images, SAM does not obtain the prior knowledge from marine images. In addition, the single-position prompt of SAM is very insufficient for prior guidance. To address these issues, we propose a novel feature learning framework, named Dual-SAM for high-performance MAS. To this end, we first introduce a dual structure with SAM's paradigm to enhance feature learning of marine images. Then, we propose a Multi-level Coupled Prompt (MCP) strategy to instruct comprehensive underwater prior information, and enhance the multi-level features of SAM's encoder with adapters. Subsequently, we design a Dilated Fusion Attention Module (DFAM) to progressively integrate multi-level features from SAM's encoder. Finally, instead of directly predicting the masks of marine animals, we propose a Criss-Cross Connectivity Prediction (C^3P) paradigm to capture the inter-connectivity between discrete pixels. With dual decoders, it generates pseudo-labels and achieves mutual supervision for complementary feature representations, resulting in considerable improvements over previous techniques. Extensive experiments verify that our proposed method achieves state-of-the-art performances on five widely-used MAS datasets. The code is available at https://github.com/Drchip61/Dual_SAM.

1. Introduction

Underwater ecosystems contain a wide variety of marine life, from microscopic plankton to colossal whales. These ecosystems are crucial roles for the earth's environmental

*Corresponding author

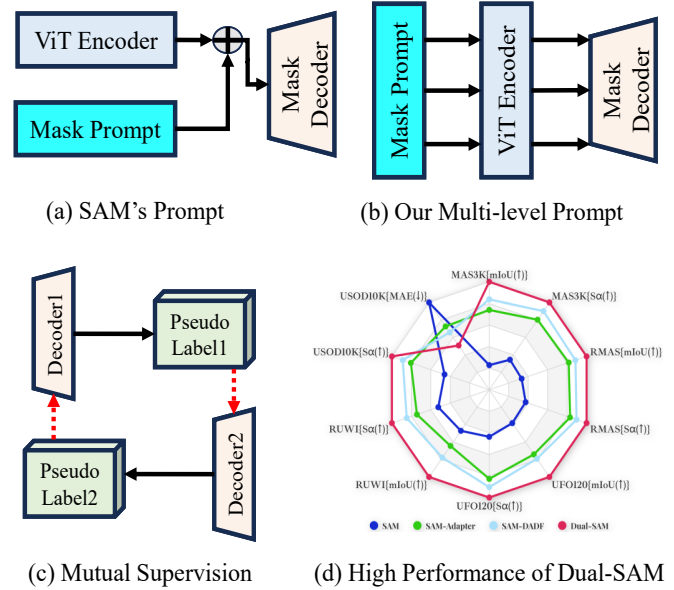


Figure 1. Our inspirations and advantages. (a) Single-position prompt of SAM. (b) Our multi-level prompt. (c) Mutual supervision for our Dual-SAM's decoders. (d) Our Dual-SAM delivers high performances on multiple datasets.

balance. Accurate and efficient Marine Animal Segmentation (MAS) is vital for understanding species' distributions, behaviors, and interactions within the submerged world. However, unlike conventional terrestrial images, underwater images include variable lighting conditions, water turbidity, color distortion, and the movement of both cameras and subjects. Traditional segmentation techniques, developed primarily for terrestrial settings, often fall short when applied to the underwater domain. Consequently, methods designed to tackle the unique aspects of the marine environment are urgently required for underwater intelligence.

With the advent of deep learning, Convolutional Neural Networks (CNNs) [18, 23] lead to a new era for image segmentation. In fact, CNNs demonstrate a remarkable ability to extract intricate features, which makes them suitable for marine animal segmentation. Nonetheless, CNNs have inherent limitations in capturing long-range dependen-

cies and contextual information within an image. Recently, Transformers [8] offer enhanced performance in capturing the long-range features of complex images. This ability is particularly appealing for underwater image segmentation, where the contextual information is often crucial to discern a marine organism from its background. However, one significant challenge for Transformers is the need of vast amounts of training data. Building on this evolution, the Segment Anything Model (SAM) [30] utilizes one billion natural images for model training. However, since the pre-training of SAM is primarily conducted under natural lighting conditions, its performance in marine environments is not optimal. In addition, the simplicity of SAM’s decoder limits its ability to capture complex details of marine organisms. Moreover, SAM introduces external prompts for instructing object priors. However, the single-position prompt is very insufficient for prior guidance.

To overcome the aforementioned issues, in this work we propose a novel feature learning framework, named Dual-SAM for high-performance MAS. Fig. 1 shows our inspirations and advantages. Technically, we first introduce a dual structure with SAM’s paradigm to enhance feature learning of marine images with gamma correction operations. Meanwhile, we enhance the multi-level features of SAM’s encoder with adapters. Then, we propose a Multi-level Coupled Prompt (MCP) strategy to instruct comprehensive underwater prior information with auto-prompts. Subsequently, we design a Dilated Fusion Attention Module (DFAM) to progressively integrate multi-level features from SAM’s encoder. Finally, instead of directly predicting the masks of marine animals, we propose a Criss-Cross Connectivity Prediction (C^3P) paradigm to capture the interconnectivity between discrete pixels. With dual decoders, it generates pseudo-labels and achieves mutual supervision for complementary feature representations. The proposed vectorized representation delivers significant improvements over previous scalar prediction techniques. Extensive experiments show that our proposed method achieves state-of-the-art performances on five widely-used MAS datasets.

In summary, our contributions are listed as follows:

- We propose a novel feature learning framework, named Dual-SAM for Marine Animal Segmentation (MAS). The framework inherits the ability of SAM and adaptively incorporates prior knowledge of underwater scenarios.
- We propose a Multi-level Coupled Prompt (MCP) strategy to instruct comprehensive underwater prior information with auto-prompts.
- We propose a Dilated Fusion Attention Module (DFAM) and a Criss-Cross Connectivity Prediction (C^3P) to improve the localization perception of marine animals.
- We perform extensive experiments to verify the effectiveness of the proposed modules. Our approach achieves a new state-of-the-art performance on five MAS datasets.

2. Related Work

2.1. Marine Animal Segmentation

MAS suffers from great challenges, such as variable lighting, particulate matter, water turbidity, etc. In past decades, most of existing methods primarily utilize handcrafted features [1, 48, 54]. Technically, energy-based models [32, 53, 60] are usually employed to predict the binary masks of marine animals. Although they achieve great success, there are still some key limitations, such as low robustness to the blurriness, unclear boundaries, etc.

With the rise of deep learning, CNNs become the preferred models for MAS. Various network architectures have been proposed to achieve performance improvements. For example, Li *et al.* [36] propose a feature-interactive encoder and a cascade decoder to extract more comprehensive information. Liu *et al.* [40] incorporate channel and spatial attention modules to refine the feature map for better object boundaries. Furthermore, Chen *et al.* [5] extract multi-scale features and introduce attention fusion blocks to highlight marine animals. Fu *et al.* [15] design a data augmentation strategy and use a Siamese structure to learn shared semantic information. Although effective, these CNN-based models lack the ability to capture long-range dependencies and intricate details for complex marine images.

Recently, Vision Transformer (ViT) [8] presents an excellent global understanding ability for multiple data types. With structural modifications, it delivers remarkable performances in various segmentation tasks [58, 70, 71, 87]. As for MAS, Hong *et al.* [20] adapt Transformer-based encoders to underwater images and show promising animal segmentation results. However, one significant challenge for Transformers is the need of vast amounts of training data. Currently, there are no very large-scale MAS datasets for the training of Transformers.

2.2. Segment Anything Model for Customized Tasks

Recently, SAM [30] is proposed to achieve universal image segmentation. It is trained on a large-scale segmentation dataset and exhibits zero-shot transfer capabilities [33, 76, 79]. With various types of prompts, it is efficiently deployed for a multitude of applications [28, 59, 83]. However, it exhibits performance limitations in transfer scenarios. In addition, the simplicity of SAM’s decoder is a hindrance when dealing with detail-aware segmentation tasks.

To address these limitations, various approaches have been proposed. Some works adopt adapters [6, 31, 78] to infuse SAM with domain-specific information. Others have opted for more specific decoder structures [16] to improve the domain perception. There are also efforts to automate the generation of prompts [3] for a better adaptability. Despite these advancements, since trained with natural images, SAM does not obtain enough prior knowledge from specific

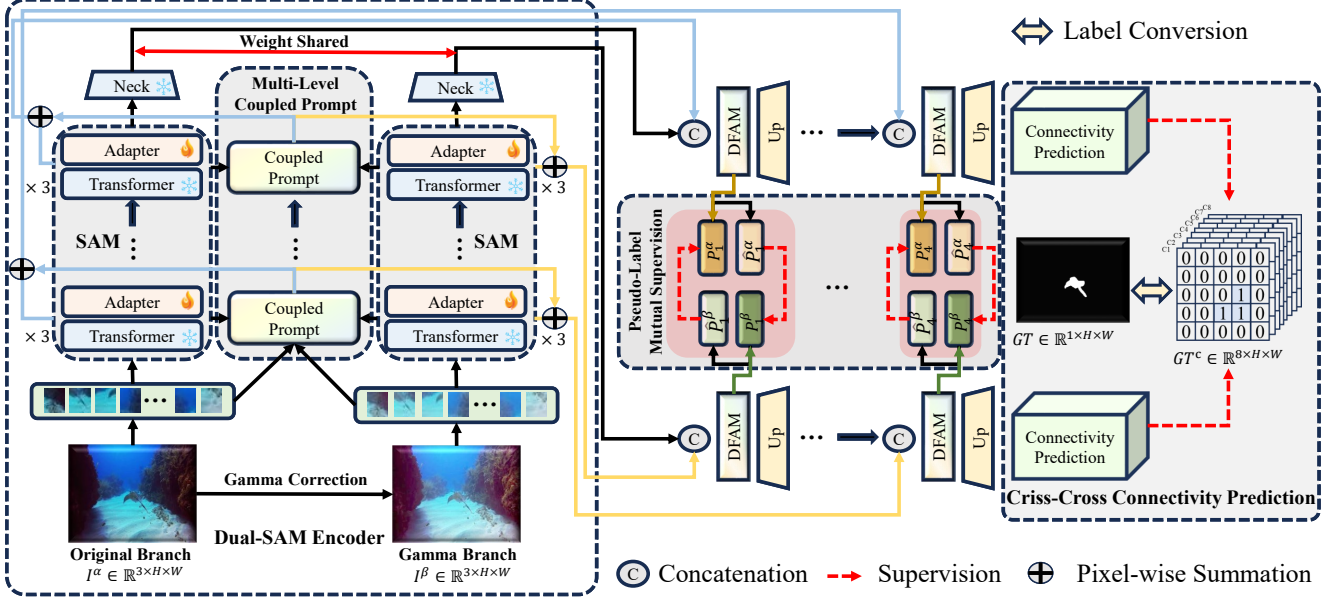


Figure 2. The whole framework of our proposed approach. It contains five main components: Dual-SAM Encoder (DSE), Multi-level Coupled Prompt (MCP), Dilated Fusion Attention Module (DFAM), Criss-Cross Connectivity Prediction (C³P) and Pseudo-label Mutual Supervision (PMS). Our framework can significantly improve the Marine Animal Segmentation (MAS) with SAM.

domains. In addition, the single-position prompt of SAM is very insufficient for prior guidance. As for MAS, we find that there is only one work [69] involving fine-tuning SAM for underwater scenes. Therefore, in this work, we delve deeply into SAM for improving the customized tasks.

3. Proposed Approach

As shown in Fig. 2, our method contains five main components: Dual-SAM Encoder (DSE), Multi-level Coupled Prompt (MCP), Dilated Fusion Attention Module (DFAM), Criss-Cross Connectivity Prediction (C³P) and Pseudo-label Mutual Supervision (PMS). These components will be elaborated in the following subsections.

3.1. Dual-SAM Encoder

As previously mentioned, it is imperative to enhance marine images with characteristics of natural images. To this end, we utilize the gamma correction for illumination compensation. Given the marine image I^α , the corrected image I^β can be expressed as:

$$I^\beta = \sqrt[\gamma]{I^\alpha}, \gamma = \lg(0.5) - \lg(\text{mean}_I^{\text{gray}}/255), \quad (1)$$

where γ is the gamma coefficient and $\text{mean}_I^{\text{gray}}$ is the mean value of the image's gray-scale intensities.

Afterwards, we inject marine domain information into SAM's encoder for a better marine feature extraction. Inspired by [6, 78], we employ low-rank trainable matrices [22] to the Query and Value portion of the Multi-Head Self-Attention (MHSA) block. In addition, we incorporate

an Adapter [21] to the Feed-Forward Network (FFN). Without loss of generality, let $X_j \in \mathbb{R}^{N \times D}$ be the output feature in the j -th layer of SAM's encoder, the feature in the $j+1$ -th layer can be represented as follows:

$$Q_j = X_j W_q + (X_j W_q^{\text{down}}) W_q^{\text{up}}, \quad (2)$$

$$K_j = X_j W_k, \quad (3)$$

$$V_j = X_j W_v + (X_j W_v^{\text{down}}) W_v^{\text{up}}, \quad (4)$$

$$H_j = \text{MHSA}(Q_j, K_j, V_j) + X_j, \quad (5)$$

$$X_{j+1} = \psi(\text{FFN}(\phi(H_j)) W^{\text{down}}) W^{\text{up}} + H_j, \quad (6)$$

where N is the total number of tokens. D is the dimension of the token embedding. $W_{q/v}^{\text{down}} \in \mathbb{R}^{D \times r}$ and $W_{q/v}^{\text{up}} \in \mathbb{R}^{r \times D}$ are linear projection matrices that reduce and subsequently restore the dimension of features, respectively. r stands for the dimension to which the features are reduced. H_i is the intermediate features within the Transformer block. Similarly, $W^{\text{down}} \in \mathbb{R}^{D \times R}$ and $W^{\text{up}} \in \mathbb{R}^{R \times D}$ are the compressed and excited operation, respectively. R stands for the compressed dimension. ψ is the GELU [19] activation function. ϕ is the layer normalization. Since we only update the linear projection matrices, it significantly reduces the number of trainable parameters for subsequent MAS tasks. With an additional branch, it can enhance animal-related features for better localizing.

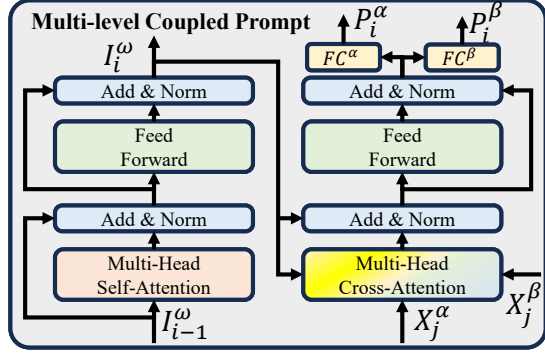


Figure 3. Our proposed Multi-level Coupled Prompt (MCP).

3.2. Multi-level Coupled Prompt

In SAM, object-related prompts (e.g., mask, box, point) are encoded and added to the feature maps. However, the single-position prompt is very insufficient for prior guidance. To improve the prompt ability, we propose a Multi-level Coupled Prompt (MCP) strategy to instruct comprehensive underwater prior information with auto-prompts.

To this end, we first concatenate the original image I^α and the corrected image I^β . Then, we partition them into patches and use convolutions to obtain feature embeddings:

$$I_0^\omega = \text{PatchEmbed}([I^\alpha, I^\beta]), \quad (7)$$

where $I_0^\omega \in \mathbb{R}^{N \times D}$ is the tokenized features, which can be served as the start point. As shown in Fig. 3, it undergoes several Transformer layers and iteratively generate features:

$$I_i^\omega = \text{Trans}(I_{i-1}^\omega), i = 1, 2, 3, 4. \quad (8)$$

Then, we treat the DSE's output features X_j^α and X_j^β as the Query and Key, respectively. By using I_i^ω as Value, we can obtain the coupled prompts as follows:

$$H_i^\tau = \text{MHCA}(X_j^\alpha, X_j^\beta, I_i^\omega) + I_i^\omega, \quad (9)$$

$$P_i^\omega = \text{FFN}(\phi(H_i^\tau)) + H_i^\tau, \quad (10)$$

$$P_i^\alpha = \text{FC}^\alpha(P_i^\omega), \quad (11)$$

$$P_i^\beta = \text{FC}^\beta(P_i^\omega), \quad (12)$$

where MHCA is the Multi-Head Cross-Attention block and FC is a fully-connected layer. The generated prompts (P_i^α and P_i^β) are coupled and can be used as auto-prompts for a better instruction and prior guidance. As a result, we can obtain prompted features by:

$$E_i^\alpha = X_j^\alpha + g_i^\alpha P_i^\alpha, \quad (13)$$

$$E_i^\beta = X_j^\beta + g_i^\beta P_i^\beta, \quad (14)$$

where g_i^α and g_i^β are learnable weights for balancing the input features and prompts.

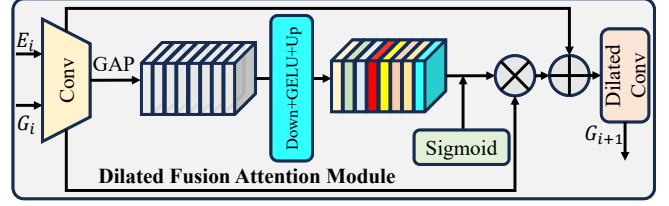


Figure 4. Our Dilated Fusion Attention Module (DFAM).

3.3. Dilated Fusion Attention Module

The simple decoder of SAM is a hindrance when dealing with complex segmentation tasks. Inspired by [37], we introduce feature pyramid structures as decoders to fuse the prompted features for MAS. To improve the receptive field, we propose the Dilated Fusion Attention Module (DFAM) with dilated convolution [4] and channel attention. It can be inserted in adjacent features (G_i and G_{i+1}). As shown in Fig. 4, the DFAM can be represented as follows:

$$F_i^r = \psi(\Theta_{1 \times 1}([E_i, G_i])), \quad (15)$$

$$W^g = \sigma(\psi(\text{GAP}(F_i^r) W^{\text{down}}) W^{\text{up}}), \quad (16)$$

$$F_i = W^g F_i^r + F_i^r, \quad (17)$$

$$G_{i+1} = \psi(\Theta_{3,3}^2(F_i)), \quad (18)$$

where σ is the sigmoid function. $\Theta_{1,1}$ is a 1×1 convolution, and $\Theta_{3,3}^2$ is a 3×3 convolution with dilation rate=2. To build the feature pyramid, we graft an up-sampling layer after the resulted features. With the above DFAM, our framework can improve the contextual perceptions of marine animals.

3.4. Criss-Cross Connectivity Prediction

Traditional image segmentation methods predict the class for each pixel. As a result, they overlook the connectivity between discrete pixels, showing irregular structures and boundaries of objects. To address this issue, we propose a Criss-Cross Connectivity Prediction (C^3P) paradigm to capture the inter-connectivity between discrete pixels. Our approach draws inspiration from [29], which emphasizes connectivity predictions between adjacent pixels. In contrast, we extend the sampling to a criss-cross range, considering various shapes and sizes of marine animals. Specifically, our method first transforms the single-channel mask label into an 8-channel label. Fig. 5 illustrates these eight channels. They represent the connectivity between their positions and the central pixel. Given a central pixel (w, h) , we identify criss-cross pixels based on the following criteria:

$$\Omega_{w,h}^1 = \{(u, v) \mid |u - w| + |v - h| = 1\}, \quad (19)$$

$$\Omega_{w,h}^2 = \{(u, v) \mid |u - w| + |v - h| = 2 \cap \text{Max}(|u - w|, |v - h|) = 2\}, \quad (20)$$

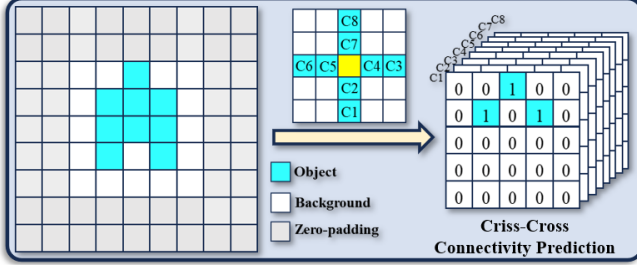


Figure 5. Our Criss-Cross Connectivity Prediction (C^3P).

where $\Omega_{w,h}^1$ and $\Omega_{w,h}^2$ are neighboring pixel sets with distances of 1 and 2, respectively. Based on above definitions, our framework directly predict connectivity maps, which provide a more comprehensive and structured representation of segmentation masks. The training loss function is:

$$\mathcal{L}_l^{\alpha/\beta} = - \sum_{w=1}^W \sum_{h=1}^H \sum_{c=1}^C [Y_l(w, h, c) \ln(P_l^{\alpha/\beta}(w, h, c)) + (1 - Y_l(w, h, c)) \ln(1 - P_l^{\alpha/\beta}(w, h, c))]. \quad (21)$$

Here, $P_l^{\alpha/\beta}$ are predicted connectivity maps at the l -th level from two decoders. It is processed after the sigmoid function. Y_l is the corresponding ground-truth. (w, h) is the spatial location of a predicted pixel. c is the channel number. As can be observed, our proposed C^3P takes the criss-cross nature of pixels and achieves vectored predictions for the animal segmentation masks.

3.5. Pseudo-label Mutual Supervision

To further ensure the comprehensive complementarity of dual branches, we employ the Pseudo-label Mutual Supervision (PMS) for the two decoders. It works like a mutual learning and enables the model to optimize its parameters from a different perspective. Specifically, we first threshold the predicted output of each level within each decoder branch. It can be represented as follows:

$$\hat{P}_l^{\alpha/\beta} = \begin{cases} 1, & P_l^{\alpha/\beta}(w, h, c) > \xi, \\ 0, & \text{otherwise.} \end{cases} \quad (22)$$

where $\hat{P}_l^{\alpha/\beta}$ are the pseudo-labels at the l -th level after thresholding. ξ is the used threshold for pseudo-labels. The above pseudo-labels are then employed to supervise the prediction of the other branch. To this end, we use the following binary cross-entropy loss functions for training:

$$\check{\mathcal{L}}_l^\alpha = - \sum_{w=1}^W \sum_{h=1}^H \sum_{c=1}^C [\hat{P}_l^\alpha(w, h, c) \ln(\hat{P}_l^\beta(w, h, c)) + (1 - \hat{P}_l^\alpha(w, h, c)) \ln(1 - \hat{P}_l^\beta(w, h, c))], \quad (23)$$

$$\check{\mathcal{L}}_l^\beta = - \sum_{w=1}^W \sum_{h=1}^H \sum_{c=1}^C [\hat{P}_l^\beta(w, h, c) \ln(\hat{P}_l^\alpha(w, h, c)) + (1 - \hat{P}_l^\beta(w, h, c)) \ln(1 - \hat{P}_l^\alpha(w, h, c))]. \quad (24)$$

Through the mutual supervision, we can foster a synergistic enhancement between the two branches, optimizing the extraction and integration of prompted features.

During the early stages of training, the connectivity predictions are very coarse and suboptimal. Thus, we introduce a dynamic update coefficient for the pseudo-label supervision. It starts at a small value, then gradually increases in an exponential manner:

$$\mu = 0.1 \times e^{-5 \times (1 - \frac{t}{T})^2}, \quad (25)$$

where t is the current epoch number during training. T is the total epochs. Finally, the overall loss is expressed as:

$$\mathcal{L} = \sum_{l=1}^4 ((\mathcal{L}_l^\alpha + \mathcal{L}_l^\beta) + \mu(\check{\mathcal{L}}_l^\alpha + \check{\mathcal{L}}_l^\beta)). \quad (26)$$

For inference, we convert the connectivity maps into the binary masks. To ensure a valid and reliable prediction, we adopt the following mutual confirmation:

$$P_{w,h,c} = 1 \cap P_{u,v,9-c} = 1 \rightarrow P_{w,h} = 1 \cap P_{u,v} = 1. \quad (27)$$

Thus, P is the final prediction for MAS.

4. Experiments

4.1. Datasets and Evaluation Metrics

To thoroughly validate the performance, we adopt five public datasets and five evaluation metrics.

For the datasets, **MAS3K** [35] contains 3,103 images with high-quality annotations. We follow the default split and use 1,769 images for training and 1,141 images for testing. We exclude 193 images that only have a background. **RMA** [15] includes 3,014 marine images. We use 2,514 images for training and 500 images for testing. **UFO120** [24] contains a total of 1,620 marine images. We use 1,500 images for training and 120 images for testing. **RUWI** [9] contains 700 marine images. We use 525 images for training and 175 images for testing. In addition, to verify the generalization, we adopt the **USOD10K** [20] dataset. It is the largest underwater salient object detection dataset with a total of 10,255 images, splitting 9,229 images for training and 1,026 images for testing.

To evaluate the model's performance, we utilize the following five metrics: Mean Intersection over Union ($mIoU$), Structural Similarity Measure (S_α), Weighted F-measure (F_β^w), Mean Enhanced-Alignment Measure (mE_ϕ), Mean Absolute Error (MAE). These metrics offer a comprehensive evaluation, capturing various aspects of segmentation quality. For more details on these metrics, please refer to the supplementary material.

Table 1. Performance comparison on MAS3K and RMAS. The best and second results are in red and blue, respectively.

Method	MAS3K					RMAS				
	mIoU	S $_{\alpha}$	F $^w_{\beta}$	mE $_{\phi}$	MAE	mIoU	S $_{\alpha}$	F $^w_{\beta}$	mE $_{\phi}$	MAE
SINet [11]	0.658	0.820	0.725	0.884	0.039	0.684	0.835	0.780	0.908	0.025
PFNet [47]	0.695	0.839	0.746	0.890	0.039	0.694	0.843	0.771	0.922	0.026
RankNet [45]	0.658	0.812	0.722	0.867	0.043	0.704	0.846	0.772	0.927	0.026
C2FNet [61]	0.717	0.851	0.761	0.894	0.038	0.721	0.858	0.788	0.923	0.026
ECDNet [36]	0.711	0.850	0.766	0.901	0.036	0.664	0.823	0.689	0.854	0.036
OCENet [38]	0.667	0.824	0.703	0.868	0.052	0.680	0.836	0.752	0.900	0.030
ZoomNet [50]	0.736	0.862	0.780	0.898	0.032	0.728	0.855	0.795	0.915	0.022
MASNet [15]	0.742	0.864	0.788	0.906	0.032	0.731	0.862	0.801	0.920	0.024
SETR [87]	0.715	0.855	0.789	0.917	0.030	0.654	0.818	0.747	0.933	0.028
TransUNet [2]	0.739	0.861	0.805	0.919	0.029	0.688	0.832	0.776	0.941	0.025
H2Former [17]	0.748	0.865	0.810	0.925	0.028	0.717	0.844	0.799	0.931	0.023
SAM [30]	0.566	0.763	0.656	0.807	0.059	0.445	0.697	0.534	0.790	0.053
SAM-Ad[6]	0.714	0.847	0.782	0.914	0.033	0.656	0.816	0.752	0.927	0.027
SAM-DA [31]	0.742	0.866	0.806	0.925	0.028	0.686	0.833	0.780	0.926	0.024
Dual-SAM	0.789	0.884	0.838	0.933	0.023	0.735	0.860	0.812	0.944	0.022

Table 2. Performance comparison on UFO120 and RUWI. The best and second results are in red and blue, respectively.

Method	UFO120					RUWI				
	mIoU	S $_{\alpha}$	F $^w_{\beta}$	mE $_{\phi}$	MAE	mIoU	S $_{\alpha}$	F $^w_{\beta}$	mE $_{\phi}$	MAE
SINet [11]	0.767	0.837	0.834	0.890	0.079	0.785	0.789	0.825	0.872	0.096
PFNet [47]	0.570	0.708	0.550	0.683	0.216	0.864	0.883	0.870	0.790	0.062
RankNet [45]	0.739	0.823	0.772	0.828	0.101	0.865	0.886	0.889	0.759	0.056
C2FNet [61]	0.747	0.826	0.806	0.878	0.083	0.840	0.830	0.883	0.924	0.060
ECDNet [36]	0.693	0.783	0.768	0.848	0.103	0.829	0.812	0.871	0.917	0.064
OCENet [38]	0.605	0.725	0.668	0.773	0.161	0.763	0.791	0.798	0.863	0.115
ZoomNet [50]	0.616	0.702	0.670	0.815	0.174	0.739	0.753	0.771	0.817	0.137
MASNet [15]	0.754	0.827	0.820	0.879	0.083	0.865	0.880	0.913	0.944	0.047
SETR [87]	0.711	0.811	0.796	0.871	0.089	0.832	0.864	0.895	0.924	0.055
TransUNet [2]	0.752	0.825	0.827	0.888	0.079	0.854	0.872	0.910	0.940	0.048
H2Former [17]	0.780	0.844	0.845	0.901	0.070	0.871	0.884	0.919	0.945	0.045
SAM [30]	0.681	0.768	0.745	0.827	0.121	0.849	0.855	0.907	0.929	0.057
SAM-Ad [6]	0.757	0.829	0.834	0.884	0.081	0.867	0.878	0.913	0.946	0.046
SAM-DA [31]	0.768	0.841	0.836	0.893	0.073	0.881	0.889	0.925	0.940	0.044
Dual-SAM	0.810	0.856	0.864	0.914	0.064	0.904	0.903	0.939	0.959	0.035

4.2. Implementation Details

We implement our model with the PyTorch toolbox and conduct experiments with one RTX 3090 GPU. In our model, the SAM’s encoder is initialized from the pre-trained SAM-B [30], while the rest are randomly initialized. During the training process, we freeze the SAM’s encoder and only fine-tune the remaining modules. To reduce the computation, we set $j = 3 \times i$ for the MCP. The threshold ξ is set to 0.5. The AdamW optimizer [44] is used to update the parameters. The initial learning rate and weight decay are set to 0.001 and 0.1, respectively. We reduce the learning rate by a factor of 10 at every 20 epochs. The total

number of training epochs T is set to 50. The mini-batch size is set to 8 due to the memory limitation. All the input images are resized to $512 \times 512 \times 3$. For the evaluation, we resize the predicted masks back to the original image size by the bilinear interpolation.

4.3. Comparisons with the State-of-the-arts

In this part, we compare our method with other methods. The quantitative and qualitative results clearly show the notable advantage of our proposed method.

Quantitative Comparisons. Tab. 9 and Tab. 10 show quantitative comparisons on typical MAS datasets. When compared with CNN-based methods, our method notably



Figure 6. Visual comparison of predicted segmentation masks with different methods.

Table 3. Performance comparison on USOD10k. The best and second results are in red and blue, respectively.

Method	USOD10K			
	S_α	mE_ϕ	maxF	MAE
S2MA [41]	.8664	.9208	.8530	.0558
SGL-KRN [68]	.9214	.9633	.9245	.0237
DCF [27]	.9116	.9541	.9045	.0312
SPNet [88]	.9075	.9554	.9069	.0280
HAINet [34]	.9123	.9552	.9116	.0279
VST [42]	.9136	.9614	.9108	.0267
TriTransNet [43]	.7889	.8479	.7501	.0659
CSNet [7]	.8595	.9178	.8462	.0548
D3Net [12]	.8931	.9413	.8807	.0374
SVAM-Net [25]	.7465	.7649	.6451	.0915
BTS-Net [80]	.9093	.9542	.9104	.0291
CDINet [74]	.7049	.8644	.7362	.0904
CTDNet [86]	.9085	.9531	.9073	.0285
MFNet [52]	.8425	.9146	.8193	.0512
PFSNet [46]	.8983	.9421	.8966	.0370
PSGLoss [72]	.8640	.9078	.8508	.0417
TC-USOD [20]	.9215	.9683	.9236	.0201
SAM [30]	.8543	.9095	.8812	.0380
SAM-Ad [6]	.8952	.9533	.9153	.0276
SAM-DA [31]	.9051	.9552	.9154	.0250
Dual-SAM	.9238	.9684	.9311	.0185

improves the performance. On the challenging MAS3K dataset, our method achieves the highest scores across all metrics. It delivers a 3-5% improvement in various metrics. Meanwhile, our method consistently performs better

on other MAS datasets. When compared with Transformer-based methods, our method delivers a 2-3% improvement on the MAS3K dataset. When compared with other SAM-based methods, our method shows a 3-4% boost in performance. Besides, in Tab. 11, we compare our method with other methods for underwater salient object detection. Our proposed method still achieves excellent results.

Qualitative Comparisons. Fig. 6 shows some visual examples to further verify the effectiveness of our method. As can be observed, our method can obtain better results in terms of whole structures (the 1st-2nd rows), multiple animals (the 3rd row), camouflage animals (the 4th row) and fine-grained boundaries (the 5th-6th rows). When compared with other SAM-based methods, our method can consistently improve the performance. The main reason is that our method introduces effective prompts and decoders.

4.4. Ablation Study

In this subsection, we conduct experiments to analyse the effect of different modules. The results are reported on the MAS3K dataset. Similar trends appear on other datasets.

Effect of Different Mask Prediction Paradigms. Tab. 4 shows the segmentation performance with different mask prediction paradigms. Clearly, the connectivity prediction delivers superior performance than the pixel-wise prediction. In predicting both pixel-level connectivity and vector-level connectivity. Our proposed C³P consistently shows better results than the connectivity prediction method [29] and pixel-wise prediction. It indicates a more comprehensive understanding of marine animals.

Table 4. Performance comparison of different prediction methods.

Method	mIoU	S_α	F_β^w	mE_ϕ	MAE
Pixel-wise	0.772	0.875	0.825	0.923	0.027
Nearby [29]	0.781	0.879	0.829	0.929	0.026
C ³ P (Ours)	0.789	0.884	0.838	0.933	0.023



Figure 7. Complementary effects of PMS on dual branch results.

Effect of Dual Branches. In this work, we introduce dual branches to improve the ability of SAM for MAS. Tab. 5 shows the performance comparison. As can be observed, the model with dual branches achieves better results than the single branch across all the metrics. It clearly demonstrates the effectiveness of our dual structures for marine feature extraction.

Effect of PMS. In this work, we employ PMS to further ensure the comprehensive complementarity of dual branches. Tab. 5 shows the performance comparison. In addition, Fig. 7 illustrates effects of the PMS. As can be observed, the performance is significantly improved by incorporating the PMS. The PMS can achieve a complementary effect in predicting segmentation masks.

Table 5. Performance comparison of dual branches and PMS.

Method	mIoU	S_α	F_β^w	mE_ϕ	MAE
Single Branch	0.767	0.872	0.816	0.922	0.028
Dual w/o PMS	0.771	0.874	0.820	0.923	0.029
Dual w PMS	0.789	0.884	0.838	0.933	0.023

Effect of MCP. In this work, we inject multi-level prompt information into SAM’s encoder for prior guidance. Tab. 6 shows the performance effect of MCP. With the proposed MCP, the model can improve the performances across all the metrics. The main reason is that the MCP helps SAM’s encoder incorporate more fine-grained information.

Effect of DFAM. In this work, we propose DFAM to fuse the prompted features. Tab. 7 provides the performance effect of DFAM. With the proposed MCP, the model can im-

Table 6. Performance effect of MCP.

Method	mIoU	S_α	F_β^w	mE_ϕ	MAE
w/o MCP	0.778	0.877	0.825	0.929	0.026
w MCP	0.789	0.884	0.838	0.933	0.023

prove the performances across all the metrics, especially in mIoU and MAE. In fact, the improved results mainly come from the dilated convolution and channel attention, which aggregate both semantic and detail information.

Table 7. Performance effect of DFAM.

Method	mIoU	S_α	F_β^w	mE_ϕ	MAE
w/o DFAM	0.769	0.873	0.821	0.921	0.028
w DFAM	0.789	0.884	0.838	0.933	0.023

Effect of Adapters. In this work, we introduce multiple adapters into the SAM’s encoder for model adaptation. Tab. 8 shows the effectiveness of different adapter mechanisms. As can be observed, the performance shows a considerable decrease when removing these adapters. These adapters play a crucial role for extracting domain-specific features. The adapters have a significant impact on each subsequent module. From the experimental results, it is evident that both types of adapters we employ can substantially and efficiently enhance the model’s performance.

Table 8. Performance comparison with different adapters.

Method	mIoU	S_α	F_β^w	mE_ϕ	MAE
Baseline	0.751	0.866	0.812	0.924	0.029
w/o LoRA [22]	0.768	0.872	0.816	0.921	0.028
w/o Adapter [21]	0.774	0.875	0.822	0.924	0.028
Full	0.789	0.884	0.838	0.933	0.023

5. Conclusion

In this paper, we propose a novel feature learning framework named Dual-SAM for MAS. The framework includes a dual structure with SAM’s paradigm to enhance feature learning of marine images. To instruct comprehensive underwater prior information, we propose a Multi-level Coupled Prompt (MCP) strategy. In addition, we design a Dilated Fusion Attention Module (DFAM) and a Criss-Cross Connectivity Prediction (C³P) to improve the localization perception of marine animals. Extensive experiments show that our proposed method achieve state-of-the-art performances on five widely-used MAS datasets.

Acknowledgements. This work was supported in part by the National Natural Science Foundation of China (No.62101092), the Fundamental Research Funds for the Central Universities (No.DUT23YG232) and the Open Project Program of State Key Laboratory of Virtual Reality Technology and Systems, Beihang University (No.VRLAB2022C02).

Fantastic Animals and Where to Find Them: Segment Any Marine Animal with Dual SAM

Supplementary Material

6. Introduction

In the main paper, we have provided quantitative comparisons with some existing methods as well as the ablation studies. In this supplementary material, we first provide details of evaluation metrics. Then, we compare our method with more methods. Afterwards, we verify the transferability and zero-shot ability of our proposed method. In addition, we further validate the effectiveness of MCP and PMS through more ablation results. Finally, we present some visual results to show the effects of key modules.

7. Evaluation Metrics

In this section, we provide details of the five evaluation metrics used to assess compared models. With these metrics, we can comprehensively and adequately demonstrate the superior performance of our model.

1) The Mean Intersection over Union (mIoU) is computed by first determining the Intersection over Union (IoU) for each individual class, and then averaging these values across all classes. It can be represented as:

$$IoU = \frac{|A \cap B|}{|A \cup B|}, mIoU = \frac{1}{C} \sum_{i=1}^C IoU_i, \quad (28)$$

where A represents the predicted values for a certain class and B represents the true values of that class.

2) The weighted F-measure (F_β^w) is determined by computing the F_β score for each class and then weighting each class’s contribution according to its occurrence frequency in the dataset. This metric can emphasize the performance on less-represented classes. It can be represented as:

$$F_\beta = \frac{(1 + \beta^2) \times Precision^\omega \times Recall^\omega}{\beta^2 \times Precision^\omega + Recall^\omega} \quad (29)$$

where $Precision$ and $Recall$ are the precision and recall scores. β is a parameter to trade-off the precision and recall. It is usually set to 0.3.

3) The structural similarity measure (S_α) [10] is a metric used to evaluate the structural similarity between two images. S_α aligns more closely with the human visual judgment of image quality.

4) The Mean Enhanced-Alignment Measure (mE_ϕ) [63] is a metric that merges local pixel information and overall image means into a single score. This metric effectively captures both the global statistics of the image and the nuances of local pixel alignments.

5) The Mean Absolute Error (MAE) quantifies the average of the absolute discrepancies between the prediction and the ground truth. It offers an overall assessment without considering class boundaries. Superior performance is reflected in lower MAE values. It can be represented as:

$$MAE(p, g) = \frac{1}{m} \sum_{i=1}^m |p_i - g_i| \quad (30)$$

where p is the prediction and g is the ground truth. m is the pixel number.

With the aforementioned five metrics, we can fully assess the overall completeness of mask predictions while ensuring the reliability of object boundaries. Therefore, achieving optimal results across these five metrics can sufficiently demonstrate the effectiveness of our model.

8. More Comparison Results

In the main paper, we compare most recent methods. Here, we present more comparison results corresponding to more methods. As shown in Tab. 9, Tab. 10 and Tab. 11, the experimental results fully demonstrate the effectiveness of our proposed method.

9. Transferability and Zero-shot Ability

In fact, our model can adapt to other complex tasks, such as saliency detection, camouflaged object detection and polyp segmentation. To verify this fact, we conduct zero-shot and transferability testing on other datasets with large domain gaps, i.e., DUTS, COD10K and Kvasir. As shown in Tab. 12, our method also achieves better results than other SAM-based methods and task-specific ones. These results clearly verify the generalization of our method. In addition, since we freeze SAM’s encoder, it somewhat preserves the zero-shot ability. As shown in Tab. 12, our method delivers comparable results with SAM, showing an expressive zero-shot ability.

10. More Ablation Results on MCP and PMS

Experiments are conducted on MAS3K [35] for its challenging and high-quality annotations.

Effects of MCP. For MCP, we first enhance the features through a self-attention mechanism, and then integrate the features extracted from SAM by using a cross-attention mechanism. In Tab. 13, we compare the effectiveness of these internal components of MCP. In the second and third rows, we list the results of using the self-attention mechanism ($S_{only}MCP$) and the cross-attention mechanism ($C_{only}MCP$), respectively. Compared with the whole MCP structure in the last row, it indicates that both mechanisms have a positive effect.

Effects of PMS. In Tab. 14, we compare the impact of using mutual supervision at different decoder layers. “1 PMS” refers to the incorporation of the mutual supervision module in the first layer of the decoder, and the other definitions follow similarly. As the number of layers increases, the performance gradually improves. We can observe that mutual supervision has a positive effect. With mutual supervision between the two branches, the objects’ details are adequately complemented.

Method	MAS3K					RMAS				
	mIoU	S_α	F_β^w	mE_ϕ	MAE	mIoU	S_α	F_β^w	mE_ϕ	MAE
UNet++ [89]	0.506	0.726	0.552	0.790	0.083	0.558	0.763	0.644	0.835	0.046
BASNet [55]	0.677	0.826	0.724	0.862	0.046	0.707	0.847	0.771	0.907	0.032
PFANet [84]	0.405	0.690	0.471	0.768	0.086	0.556	0.767	0.582	0.810	0.051
SCRN [67]	0.693	0.839	0.730	0.869	0.041	0.695	0.842	0.731	0.878	0.030
U2Net [56]	0.654	0.812	0.711	0.851	0.047	0.676	0.830	0.762	0.904	0.029
SINet [11]	0.658	0.820	0.725	0.884	0.039	0.684	0.835	0.780	0.908	0.025
PFNet [47]	0.695	0.839	0.746	0.890	0.039	0.694	0.843	0.771	0.922	0.026
RankNet [45]	0.658	0.812	0.722	0.867	0.043	0.704	0.846	0.772	0.927	0.026
C2FNet [61]	0.717	0.851	0.761	0.894	0.038	0.721	0.858	0.788	0.923	0.026
ECDNet [36]	0.711	0.850	0.766	0.901	0.036	0.664	0.823	0.689	0.854	0.036
OCENet [38]	0.667	0.824	0.703	0.868	0.052	0.680	0.836	0.752	0.900	0.030
ZoomNet [50]	0.736	0.862	0.780	0.898	0.032	0.728	0.855	0.795	0.915	0.022
MASNet [15]	0.742	0.864	0.788	0.906	0.032	0.731	0.862	0.801	0.920	0.024
SETR [87]	0.715	0.855	0.789	0.917	0.030	0.654	0.818	0.747	0.933	0.028
TransUNet [2]	0.739	0.861	0.805	0.919	0.029	0.688	0.832	0.776	0.941	0.025
H2Former [17]	0.748	0.865	0.810	0.925	0.028	0.717	0.844	0.799	0.931	0.023
SAM [30]	0.566	0.763	0.656	0.807	0.059	0.445	0.697	0.534	0.790	0.053
SAM-Adapter[6]	0.714	0.847	0.782	0.914	0.033	0.656	0.816	0.752	0.927	0.027
SAM-DADF [31]	0.742	0.866	0.806	0.925	0.028	0.686	0.833	0.780	0.926	0.024
Dual-SAM	0.789	0.884	0.838	0.933	0.023	0.735	0.860	0.812	0.944	0.022

Table 9. Performance comparison on MAS3K and RMAS. The best and second results are in red and blue, respectively.

Method	UFO120					RUWI				
	mIoU	S_α	F_β^w	mE_ϕ	MAE	mIoU	S_α	F_β^w	mE_ϕ	MAE
UNet++ [89]	0.412	0.459	0.433	0.451	0.409	0.586	0.714	0.678	0.790	0.145
BASNet [55]	0.710	0.809	0.793	0.865	0.097	0.841	0.871	0.895	0.922	0.056
PFANet [84]	0.677	0.752	0.723	0.815	0.129	0.773	0.765	0.811	0.867	0.096
SCRN [67]	0.678	0.783	0.760	0.839	0.106	0.830	0.847	0.883	0.925	0.059
U2Net [56]	0.680	0.792	0.709	0.811	0.134	0.841	0.873	0.861	0.786	0.074
SINet [11]	0.767	0.837	0.834	0.890	0.079	0.785	0.789	0.825	0.872	0.096
PFNet [47]	0.570	0.708	0.550	0.683	0.216	0.864	0.883	0.870	0.790	0.062
RankNet [45]	0.739	0.823	0.772	0.828	0.101	0.865	0.886	0.889	0.759	0.056
C2FNet [61]	0.747	0.826	0.806	0.878	0.083	0.840	0.830	0.883	0.924	0.060
ECDNet [36]	0.693	0.783	0.768	0.848	0.103	0.829	0.812	0.871	0.917	0.064
OCENet [38]	0.605	0.725	0.668	0.773	0.161	0.763	0.791	0.798	0.863	0.115
ZoomNet [50]	0.616	0.702	0.670	0.815	0.174	0.739	0.753	0.771	0.817	0.137
MASNet [15]	0.754	0.827	0.820	0.879	0.083	0.865	0.880	0.913	0.944	0.047
SETR [87]	0.711	0.811	0.796	0.871	0.089	0.832	0.864	0.895	0.924	0.055
TransUNet [2]	0.752	0.825	0.827	0.888	0.079	0.854	0.872	0.910	0.940	0.048
H2Former [17]	0.780	0.844	0.845	0.901	0.070	0.871	0.884	0.919	0.945	0.045
SAM [30]	0.681	0.768	0.745	0.827	0.121	0.849	0.855	0.907	0.929	0.057
SAM-Adapter [6]	0.757	0.829	0.834	0.884	0.081	0.867	0.878	0.913	0.946	0.046
SAM-DADF [31]	0.768	0.841	0.836	0.893	0.073	0.881	0.889	0.925	0.940	0.044
Dual-SAM	0.810	0.856	0.864	0.914	0.064	0.904	0.903	0.939	0.959	0.035

Table 10. Performance comparison on UFO120 and RUWI. The best and second results are in red and blue, respectively.

Method	USOD10k			
	S_α	mE_ϕ	maxF	MAE
Itti [26]	.6112	.6670	.4676	.1798
RCRR [73]	.6449	.6898	.5592	.1831
DF [57]	.6410	.7576	.5589	.1400
CPD [66]	.9076	.9484	.8991	.0290
DMRA [51]	.8746	.9274	.8682	.0422
SAMNet [84]	.8875	.9382	.8739	.0396
PoolNet [39]	.9152	.9562	.9105	.0283
BASNet [55]	.9075	.9378	.8849	.0352
EGNet [82]	.9125	.9488	.9040	.0291
FC-SOD [75]	.7036	.7004	.6231	.0852
LDF [65]	.9135	.9574	.9173	.0260
F3Net [64]	.9140	.9599	.9171	.0251
PFPN [62]	.9090	.9547	.9055	.0302
MINet [49]	.9105	.9501	.9072	.0287
DASNet [81]	.9204	.9603	.9212	.0245
JL-DCF [14]	.9062	.9485	.8978	.0300
UCNet [77]	.8997	.9463	.8968	.0301
S2MA [41]	.8664	.9208	.8530	.0558
BBSNet [13]	.9061	.9512	.9056	.0337
DANet [85]	.9006	.9449	.8934	.0279
SGL-KRN [68]	.9214	.9633	.9245	.0237
DCF [27]	.9116	.9541	.9045	.0312
SPNet [88]	.9075	.9554	.9069	.0280
HAINet [34]	.9123	.9552	.9116	.0279
VST [42]	.9136	.9614	.9108	.0267
TriTransNet [43]	.7889	.8479	.7501	.0659
CSNet [7]	.8595	.9178	.8462	.0548
D3Net [12]	.8931	.9413	.8807	.0374
SVAM-Net [25]	.7465	.7649	.6451	.0915
BTS-Net [80]	.9093	.9542	.9104	.0291
CDINet [74]	.7049	.8644	.7362	.0904
CTDNet [86]	.9085	.9531	.9073	.0285
MFNet [52]	.8425	.9146	.8193	.0512
PFSNet [46]	.8983	.9421	.8966	.0370
PSGLoss [72]	.8640	.9078	.8508	.0417
TC-USOD [20]	.9215	.9683	.9236	.0201
SAM [30]	.8543	.9095	.8812	.0380
SAM-Adapter [6]	.8952	.9533	.9153	.0276
SAM-DADF [31]	.9051	.9552	.9154	.0250
Dual-SAM	.9238	.9684	.9311	.0185

Table 11. Performance comparison on USOD10k. The best and second results are in red and blue, respectively.

11. More Visual Results

In the main paper, we have already presented a visual comparison of typical methods. In this supplementary material, we provide more visual results to verify the effects of our proposed key modules.

Visual Results with Key Modules. In Fig. 8, we show the visual effect of our C^3P module. One can observe that our C^3P

Method	DUTS (SOD)		COD10K (COD)		Kvasir (Medical)	
	F_β^w	MAE	F_β^w	MAE	F_β^w	MAE
VST	0.828	0.037	—	—	—	—
PFNet	—	—	0.660	0.040	—	—
FAPNet	—	—	—	—	0.894	0.027
SAM	0.764	0.058	0.633	0.050	0.769	0.062
SAM-Adapter	0.878	0.029	0.801	0.025	0.876	0.029
Ours (zero-shot)	0.783	0.048	0.677	0.044	0.696	0.082
Ours	0.885	0.025	0.889	0.012	0.909	0.025

Table 12. Performance comparison on other complex tasks.

Method	mIoU	S_α	F_β^w	mE_ϕ	MAE
no MCP	0.778	0.877	0.825	0.929	0.026
S_{only} MCP	0.779	0.878	0.828	0.931	0.026
C_{only} MCP	0.783	0.879	0.832	0.931	0.025
MCP	0.789	0.884	0.838	0.933	0.023

Table 13. Performance comparisons of MCP.

Method	mIoU	S_α	F_β^w	mE_ϕ	MAE
no PMS	0.771	0.874	0.820	0.923	0.029
1 PMS	0.776	0.876	0.823	0.926	0.027
2 PMS	0.779	0.878	0.827	0.927	0.026
3 PMS	0.783	0.880	0.830	0.932	0.025
4 PMS	0.789	0.884	0.838	0.933	0.023

Table 14. Performance comparisons with different layers of PMS.

module helps to obtain a better overall shape of underwater targets. The binary cross-entropy loss and nearby connectivity prediction are not good at predicting the animal boundaries In Fig. 9, we show the visual effect of our PMS module. By employing dual branches for mutual supervision, the segmentation maps have comprehensive information, effectively removing redundant information. In Fig. 10, we show the visual effect of our MCP module. With the multi-level coupled guidance, SAM has gained enhanced representational capabilities for animals and suppressed the cluttered backgrounds. In Fig. 11, we show the visual effect of our DFAM module. We integrate the features extracted from both the encoder and decoder through the DFAM module, and select more important feature channels. The design can adaptively aggregate more contextual information and significantly improve the segmentation results. In Fig. 12, we show the visual effect of our adapter mechanism. One can observe that our method effectively injects underwater domain information into the SAM backbone. Furthermore, the use of our dual adapter mechanisms continues to have a positive impact on the performance.

Visualization of Failed Results. In Fig. 13, we present some failure cases. Due to the similarity between the animal and its environment, it is challenging for our model to capture it accurately. However, other existing methods also result in significant segmentation errors. Therefore, distinguishing such organisms has become a focus of our further efforts.

References

- [1] Herbert Bay, Andreas Ess, Tinne Tuytelaars, and Luc Van Gool. Speeded-up robust features (surf). *CVIU*, 110(3):346–359, 2008. 2

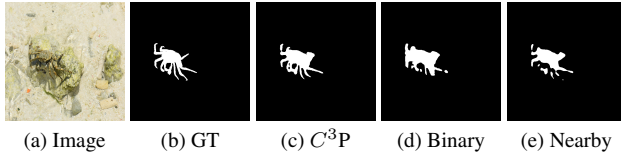


Figure 8. Visualizing the effect of our C^3P module.

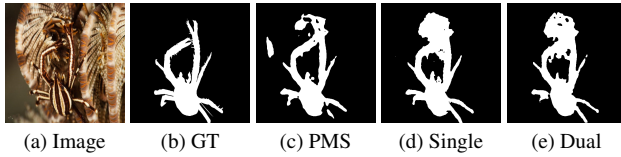


Figure 9. Visualizing the effect of our PMS module.

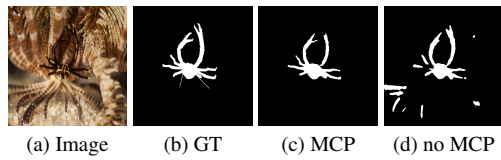


Figure 10. Visualizing the effect of our MCP module.

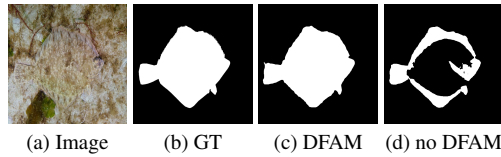


Figure 11. Visualizing the effect of our DFAM module.

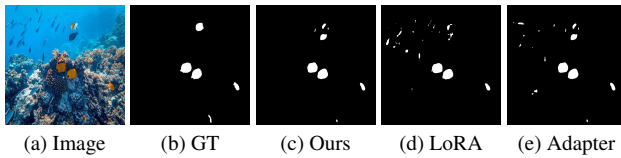


Figure 12. Visualizing the effect of different adapter mechanisms.

- [2] Jieneng Chen, Yongyi Lu, Qihang Yu, Xiangde Luo, Ehsan Adeli, Yan Wang, Le Lu, Alan L Yuille, and Yuyin Zhou. Transunet: Transformers make strong encoders for medical image segmentation. *arXiv*, 2021. **6, 2**
- [3] Keyan Chen, Chenyang Liu, Hao Chen, Haotian Zhang, Wenyuan Li, Zhengxia Zou, and Zhenwei Shi. Rsprompter: Learning to prompt for remote sensing instance segmentation based on visual foundation model. *arXiv*, 2023. **2**
- [4] Liang-Chieh Chen, George Papandreou, Iasonas Kokkinos, Kevin Murphy, and Alan L Yuille. Deeplab: Semantic image segmentation with deep convolutional nets, atrous convolution, and fully connected crfs. *IEEE TPAMI*, 40(4):834–848, 2017. **4**
- [5] Ruizhe Chen, Zhenqi Fu, Yue Huang, En Cheng, and Xinghao Ding. A robust object segmentation network for underwater scenes. In *ICASSP*, pages 2629–2633. IEEE, 2022. **2**
- [6] Tianrun Chen, Lanyun Zhu, Chaotao Ding, Runlong Cao, Shangzhan Zhang, Yan Wang, Zejian Li, Lingyun Sun, Papa Mao, and Ying Zang. Sam fails to segment anything?—sam-adapter: Adapting sam in underperformed scenes: Camouflage, shadow, and more. *arXiv*, 2023. **2, 3, 6, 7**
- [7] Ming-Ming Cheng, Shang-Hua Gao, Ali Borji, Yong-Qiang Tan, Zheng Lin, and Meng Wang. A highly efficient model to study the semantics of salient object detection. *PAMI*, 44(11):8006–8021, 2021. **7, 3**
- [8] Alexey Dosovitskiy, Lucas Beyer, Alexander Kolesnikov, Dirk Weissenborn, Xiaohua Zhai, Thomas Unterthiner, Mostafa Dehghani, Matthias Minderer, Georg Heigold, Sylvain Gelly, et al. An image is worth 16x16 words: Transformers for image recognition at scale. *arXiv*, 2020. **2**
- [9] Paulo Dreuws-Jr, Isadora de Souza, Igor P Maurell, Eglen V Protas, and Silvia S C. Botelho. Underwater image segmentation in the wild using deep learning. *Journal of the Brazilian Computer Society*, 27:1–14, 2021. **5**
- [10] Deng-Ping Fan, Cheng Gong, Yang Cao, Bo Ren, Ming-Ming Cheng, and Ali Borji. Enhanced-alignment measure for binary foreground map evaluation. *arXiv preprint arXiv:1805.10421*, 2018. **1**
- [11] Deng-Ping Fan, Ge-Peng Ji, Guolei Sun, Ming-Ming Cheng, Jianbing Shen, and Ling Shao. Camouflaged object detection. In *CVPR*, pages 2777–2787, 2020. **6, 2**
- [12] Deng-Ping Fan, Zheng Lin, Zhao Zhang, Menglong Zhu, and Ming-Ming Cheng. Rethinking rgb-d salient object detection: Models, data sets, and large-scale benchmarks. *TNNLS*, 32(5):2075–2089, 2020. **7, 3**
- [13] Deng-Ping Fan, Yingjie Zhai, Ali Borji, Jufeng Yang, and Ling Shao. Bbs-net: Rgb-d salient object detection with a bifurcated backbone strategy network. In *ECCV*, pages 275–292. Springer, 2020. **3**
- [14] Keren Fu, Deng-Ping Fan, Ge-Peng Ji, and Qijun Zhao. Jldcf: Joint learning and densely-cooperative fusion framework for rgb-d salient object detection. In *CVPR*, pages 3052–3062, 2020. **3**
- [15] Zhenqi Fu, Ruizhe Chen, Yue Huang, En Cheng, Xinghao Ding, and Kai-Kuang Ma. Masnet: A robust deep marine animal segmentation network. *IEEE Journal of Oceanic Engineering*, 2023. **2, 5, 6**
- [16] Yifan Gao, Wei Xia, Dingdu Hu, and Xin Gao. Desam: Decoupling segment anything model for generalizable medical image segmentation. *arXiv*, 2023. **2**
- [17] Along He, Kai Wang, Tao Li, Chengkun Du, Shuang Xia, and Huazhu Fu. H2former: An efficient hierarchical hybrid transformer for medical image segmentation. *TMI*, 2023. **6, 2**
- [18] Kaiming He, Xiangyu Zhang, Shaoqing Ren, and Jian Sun. Deep residual learning for image recognition. In *CVPR*, pages 770–778, 2016. **1**
- [19] Dan Hendrycks and Kevin Gimpel. Gaussian error linear units (gelus). *arXiv preprint arXiv:1606.08415*, 2016. **3**
- [20] Lin Hong, Xin Wang, Gan Zhang, and Ming Zhao. Usod10k: a new benchmark dataset for underwater salient object detection. *TIP*, 2023. **2, 5, 7, 3**

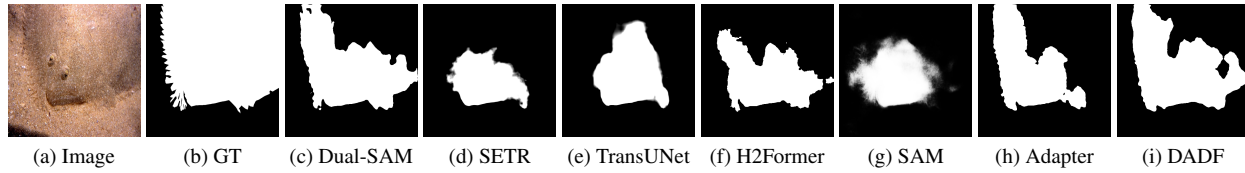


Figure 13. Visualizing failure segmentation cases.

- [21] Neil Houlsby, Andrei Giurgiu, Stanislaw Jastrzebski, Bruna Morrone, Quentin De Laroussilhe, Andrea Gesmundo, Mona Attariyan, and Sylvain Gelly. Parameter-efficient transfer learning for nlp. In *ICML*, pages 2790–2799. PMLR, 2019. [3](#), [8](#)
- [22] Edward J Hu, Yelong Shen, Phillip Wallis, Zeyuan Allen-Zhu, Yuanzhi Li, Shean Wang, Lu Wang, and Weizhu Chen. Lora: Low-rank adaptation of large language models. *arXiv*, 2021. [3](#), [8](#)
- [23] Gao Huang, Zhuang Liu, Laurens Van Der Maaten, and Kilian Q Weinberger. Densely connected convolutional networks. In *CVPR*, pages 4700–4708, 2017. [1](#)
- [24] Md Jahidul Islam, Peigen Luo, and Junaed Sattar. Simultaneous enhancement and super-resolution of underwater imagery for improved visual perception. *arXiv*, 2020. [5](#)
- [25] Md Jahidul Islam, Ruobing Wang, and Junaed Sattar. Svam: saliency-guided visual attention modeling by autonomous underwater robots. *arXiv*, 2020. [7](#), [3](#)
- [26] Laurent Itti, Christof Koch, and Ernst Niebur. A model of saliency-based visual attention for rapid scene analysis. *PAMI*, 20(11):1254–1259, 1998. [3](#)
- [27] Wei Ji, Jingjing Li, Shuang Yu, Miao Zhang, Yongri Piao, Shunyu Yao, Qi Bi, Kai Ma, Yefeng Zheng, Huchuan Lu, et al. Calibrated rgb-d salient object detection. In *CVPR*, pages 9471–9481, 2021. [7](#), [3](#)
- [28] Zheyang Jin, Shiqi Chen, Yueting Chen, Zhihai Xu, and Hua-jun Feng. Let segment anything help image dehaze. *arXiv*, 2023. [2](#)
- [29] Michael Kampffmeyer, Nanqing Dong, Xiaodan Liang, Yujia Zhang, and Eric P Xing. Connet: A long-range relation-aware pixel-connectivity network for salient segmentation. *TIP*, 28(5):2518–2529, 2018. [4](#), [7](#), [8](#)
- [30] Alexander Kirillov, Eric Mintun, Nikhila Ravi, Hanzi Mao, Chloe Rolland, Laura Gustafson, Tete Xiao, Spencer Whitehead, Alexander C Berg, Wan-Yen Lo, et al. Segment anything. *arXiv*, 2023. [2](#), [6](#), [7](#), [3](#)
- [31] Yingxin Lai, Zhiming Luo, and Zitong Yu. Detect any deep-fakes: Segment anything meets face forgery detection and localization. *arXiv*, 2023. [2](#), [6](#), [7](#), [3](#)
- [32] David M Lane, Mike J Chantler, and Dongyong Dai. Robust tracking of multiple objects in sector-scan sonar image sequences using optical flow motion estimation. *IEEE Journal of Oceanic Engineering*, 23(1):31–46, 1998. [2](#)
- [33] Wenhui Lei, Xu Wei, Xiaofan Zhang, Kang Li, and Shaoting Zhang. Medlsam: Localize and segment anything model for 3d medical images. *arXiv*, 2023. [2](#)
- [34] Gongyang Li, Zhi Liu, Minyu Chen, Zhen Bai, Weisi Lin, and Haibin Ling. Hierarchical alternate interaction network for rgb-d salient object detection. *TIP*, 30:3528–3542, 2021. [7](#), [3](#)
- [35] Lin Li, Eric Rigall, Junyu Dong, and Geng Chen. Mas3k: An open dataset for marine animal segmentation. In *International Symposium on Benchmarking, Measuring and Optimization*, pages 194–212. Springer, 2020. [5](#), [1](#)
- [36] Lin Li, Bo Dong, Eric Rigall, Tao Zhou, Junyu Dong, and Geng Chen. Marine animal segmentation. *TCSVT*, 32(4): 2303–2314, 2021. [2](#), [6](#)
- [37] Tsung-Yi Lin, Piotr Dollár, Ross Girshick, Kaiming He, Bharath Hariharan, and Serge Belongie. Feature pyramid networks for object detection. In *ICCV*, pages 2117–2125, 2017. [4](#)
- [38] Jiawei Liu, Jing Zhang, and Nick Barnes. Modeling aleatoric uncertainty for camouflaged object detection. In *WACV*, pages 1445–1454, 2022. [6](#), [2](#)
- [39] Jiang-Jiang Liu, Qibin Hou, Ming-Ming Cheng, Jiashi Feng, and Jianmin Jiang. A simple pooling-based design for real-time salient object detection. In *CVPR*, pages 3917–3926, 2019. [3](#)
- [40] Lidan Liu and Weiwei Yu. Underwater image saliency detection via attention-based mechanism. In *Journal of Physics: Conference Series*, page 012012. IOP Publishing, 2022. [2](#)
- [41] Nian Liu, Ni Zhang, Ling Shao, and Junwei Han. Learning selective mutual attention and contrast for rgb-d saliency detection. *TPAMI*, 44(12):9026–9042, 2021. [7](#), [3](#)
- [42] Ze Liu, Yutong Lin, Yue Cao, Han Hu, Yixuan Wei, Zheng Zhang, Stephen Lin, and Baining Guo. Swin transformer: Hierarchical vision transformer using shifted windows. In *ICCV*, pages 10012–10022, 2021. [7](#), [3](#)
- [43] Zhengyi Liu, Yuan Wang, Zhengzheng Tu, Yun Xiao, and Bin Tang. Tritransnet: Rgb-d salient object detection with a triplet transformer embedding network. In *ACMMM*, pages 4481–4490, 2021. [7](#), [3](#)
- [44] Ilya Loshchilov and Frank Hutter. Decoupled weight decay regularization. *arXiv*, 2017. [6](#)
- [45] Yunqiu Lv, Jing Zhang, Yuchao Dai, Aixuan Li, Bowen Liu, Nick Barnes, and Deng-Ping Fan. Simultaneously localize, segment and rank the camouflaged objects. In *CVPR*, pages 11591–11601, 2021. [6](#), [2](#)
- [46] Mingcan Ma, Changqun Xia, and Jia Li. Pyramidal feature shrinking for salient object detection. In *AAAI*, pages 2311–2318, 2021. [7](#), [3](#)
- [47] Haiyang Mei, Ge-Peng Ji, Ziqi Wei, Xin Yang, Xiaopeng Wei, and Deng-Ping Fan. Camouflaged object segmentation with distraction mining. In *CVPR*, pages 8772–8781, 2021. [6](#), [2](#)

- [48] Pauline C Ng and Steven Henikoff. Sift: Predicting amino acid changes that affect protein function. *NAS*, 31(13):3812–3814, 2003. 2
- [49] Youwei Pang, Xiaoqi Zhao, Lihe Zhang, and Huchuan Lu. Multi-scale interactive network for salient object detection. In *CVPR*, pages 9413–9422, 2020. 3
- [50] Youwei Pang, Xiaoqi Zhao, Tian-Zhu Xiang, Lihe Zhang, and Huchuan Lu. Zoom in and out: A mixed-scale triplet network for camouflaged object detection. In *CVPR*, pages 2160–2170, 2022. 6, 2
- [51] Yongri Piao, Wei Ji, Jingjing Li, Miao Zhang, and Huchuan Lu. Depth-induced multi-scale recurrent attention network for saliency detection. In *ICCV*, pages 7254–7263, 2019. 3
- [52] Yongri Piao, Jian Wang, Miao Zhang, and Huchuan Lu. Mfnet: Multi-filter directive network for weakly supervised salient object detection. In *ICCV*, pages 4136–4145, 2021. 7, 3
- [53] Divya Priyadarshni and Mahesh Kumar H Kolekar. Underwater object detection and tracking. In *Soft Computing*, pages 837–846. Springer, 2020. 2
- [54] R Priyadharsini and T Sree Sharmila. Object detection in underwater acoustic images using edge based segmentation method. *Procedia Computer Science*, 165:759–765, 2019. 2
- [55] Xuebin Qin, Zichen Zhang, Chenyang Huang, Chao Gao, Masood Dehghan, and Martin Jagersand. Basnet: Boundary-aware salient object detection. In *CVPR*, pages 7479–7489, 2019. 2, 3
- [56] Xuebin Qin, Zichen Zhang, Chenyang Huang, Masood Dehghan, Osmar R Zaiane, and Martin Jagersand. U2-net: Going deeper with nested u-structure for salient object detection. *PR*, 106:107404, 2020. 2
- [57] Liangqiong Qu, Shengfeng He, Jiawei Zhang, Jiandong Tian, Yandong Tang, and Qingxiong Yang. Rgb-d salient object detection via deep fusion. *TIP*, 26(5):2274–2285, 2017. 3
- [58] René Ranftl, Alexey Bochkovskiy, and Vladlen Koltun. Vision transformers for dense prediction. In *ICCV*, pages 12179–12188, 2021. 2
- [59] Xinru Shan and Chaoning Zhang. Robustness of segment anything model (sam) for autonomous driving in adverse weather conditions. *arXiv*, 2023. 2
- [60] ASM Shihavuddin, Nuno Gracias, Rafael Garcia, Javier Escartin, and Rolf Birger Pedersen. Automated classification and thematic mapping of bacterial mats in the north sea. In *OCEANS*, pages 1–8. IEEE, 2013. 2
- [61] Yujia Sun, Geng Chen, Tao Zhou, Yi Zhang, and Nian Liu. Context-aware cross-level fusion network for camouflaged object detection. *arXiv*, 2021. 6, 2
- [62] Bo Wang, Quan Chen, Min Zhou, Zhiqiang Zhang, Xiaogang Jin, and Kun Gai. Progressive feature polishing network for salient object detection. In *AAAI*, pages 12128–12135, 2020. 3
- [63] Zhou Wang, Alan C Bovik, Hamid R Sheikh, and Eero P Simoncelli. Image quality assessment: from error visibility to structural similarity. *IEEE TIP*, 13(4):600–612, 2004. 1
- [64] Jun Wei, Shuhui Wang, and Qingming Huang. F³net: fusion, feedback and focus for salient object detection. In *AAAI*, pages 12321–12328, 2020. 3
- [65] Jun Wei, Shuhui Wang, Zhe Wu, Chi Su, Qingming Huang, and Qi Tian. Label decoupling framework for salient object detection. In *CVPR*, pages 13025–13034, 2020. 3
- [66] Zhe Wu, Li Su, and Qingming Huang. Cascaded partial decoder for fast and accurate salient object detection. In *CVPR*, pages 3907–3916, 2019. 3
- [67] Zhe Wu, Li Su, and Qingming Huang. Stacked cross refinement network for edge-aware salient object detection. In *ICCV*, pages 7264–7273, 2019. 2
- [68] Binwei Xu, Haoran Liang, Ronghua Liang, and Peng Chen. Locate globally, segment locally: A progressive architecture with knowledge review network for salient object detection. In *AAAI*, pages 3004–3012, 2021. 7, 3
- [69] Muduo Xu, Jianhao Su, and Yutao Liu. Aquasam: Underwater image foreground segmentation. *arXiv*, 2023. 3
- [70] Tianyu Yan, Zifu Wan, and Pingping Zhang. Fully transformer network for change detection of remote sensing images. In *ACCV*, pages 1691–1708, 2022. 2
- [71] Tianyu Yan, Zifu Wan, Pingping Zhang, Gong Cheng, and Huchuan Lu. Transy-net: Learning fully transformer networks for change detection of remote sensing images. *TGRS*, 61:1–12, 2023. 2
- [72] Sheng Yang, Weisi Lin, Guosheng Lin, Qiuping Jiang, and Zichuan Liu. Progressive self-guided loss for salient object detection. *TIP*, 30:8426–8438, 2021. 7, 3
- [73] Yuchen Yuan, Changyang Li, Jinman Kim, Weidong Cai, and David Dagan Feng. Reversion correction and regularized random walk ranking for saliency detection. *TIP*, 27(3): 1311–1322, 2017. 3
- [74] Chen Zhang, Runmin Cong, Qinwei Lin, Lin Ma, Feng Li, Yao Zhao, and Sam Kwong. Cross-modality discrepant interaction network for rgb-d salient object detection. In *ACMMM*, pages 2094–2102, 2021. 7, 3
- [75] Dingwen Zhang, Haibin Tian, and Jungong Han. Few-cost salient object detection with adversarial-paced learning. *ANIPS*, 33:12236–12247, 2020. 3
- [76] Dingyuan Zhang, Dingkan Liang, Hongcheng Yang, Zhikang Zou, Xiaoqing Ye, Zhe Liu, and Xiang Bai. Sam3d: Zero-shot 3d object detection via segment anything model. *arXiv*, 2023. 2
- [77] Jing Zhang, Deng-Ping Fan, Yuchao Dai, Saeed Anwar, Fatemeh Sadat Saleh, Tong Zhang, and Nick Barnes. Uc-net: Uncertainty inspired rgb-d saliency detection via conditional variational autoencoders. In *CVPR*, pages 8582–8591, 2020. 3
- [78] Kaidong Zhang and Dong Liu. Customized segment anything model for medical image segmentation. *arXiv*, 2023. 2, 3
- [79] Lian Zhang, Zhengliang Liu, Lu Zhang, Zihao Wu, Xiaowei Yu, Jason Holmes, Hongying Feng, Haixing Dai, Xiang Li, Quanzheng Li, et al. Segment anything model (sam) for radiation oncology. *arXiv*, 2023. 2
- [80] Wenbo Zhang, Yao Jiang, Keren Fu, and Qijun Zhao. Bts-net: Bi-directional transfer-and-selection network for rgb-d salient object detection. In *ICME*, pages 1–6. IEEE, 2021. 7, 3

- [81] Jiawei Zhao, Yifan Zhao, Jia Li, and Xiaowu Chen. Is depth really necessary for salient object detection? In *ACMMM*, pages 1745–1754, 2020. [3](#)
- [82] Jia-Xing Zhao, Jiang-Jiang Liu, Deng-Ping Fan, Yang Cao, Jufeng Yang, and Ming-Ming Cheng. Egnnet: Edge guidance network for salient object detection. In *ICCV*, pages 8779–8788, 2019. [3](#)
- [83] Qihan Zhao, Xiaofeng Zhang, Hao Tang, Chaochen Gu, and Shanying Zhu. Enlighten-anything: When segment anything model meets low-light image enhancement. *arXiv*, 2023. [2](#)
- [84] Ting Zhao and Xiangqian Wu. Pyramid feature attention network for saliency detection. In *CVPR*, pages 3085–3094, 2019. [2](#), [3](#)
- [85] Xiaoqi Zhao, Lihe Zhang, Youwei Pang, Huchuan Lu, and Lei Zhang. A single stream network for robust and real-time rgb-d salient object detection. In *ECCV*, pages 646–662. Springer, 2020. [3](#)
- [86] Zhirui Zhao, Changqun Xia, Chenxi Xie, and Jia Li. Complementary trilateral decoder for fast and accurate salient object detection. In *ACMMM*, pages 4967–4975, 2021. [7](#), [3](#)
- [87] Sixiao Zheng, Jiachen Lu, Hengshuang Zhao, Xiatian Zhu, Zekun Luo, Yabiao Wang, Yanwei Fu, Jianfeng Feng, Tao Xiang, Philip HS Torr, et al. Rethinking semantic segmentation from a sequence-to-sequence perspective with transformers. In *CVPR*, pages 6881–6890, 2021. [2](#), [6](#)
- [88] Tao Zhou, Huazhu Fu, Geng Chen, Yi Zhou, Deng-Ping Fan, and Ling Shao. Specificity-preserving rgb-d saliency detection. In *ICCV*, pages 4681–4691, 2021. [7](#), [3](#)
- [89] Zongwei Zhou, Md Mahfuzur Rahman Siddiquee, Nima Tajbakhsh, and Jianming Liang. Unet++: A nested u-net architecture for medical image segmentation. In *MICCAI*, pages 3–11. Springer, 2018. [2](#)